An artificial molecular switch that mimics the visual pigment and completes its photocycle in picoseconds

Adalgisa Sinicropi[a], Elena Martin[b], Mikhail Ryazantsev[c], Jan Helbing[d,1], Julien Briand[e], Divya Sharma[e], Jérémie Léonard[e], Stefan Haacke[e,1], Andrea Cannizzo[f], Majed Chergui[f], Vinicio Zanirato[g], Stefania Fusi[a], Fabrizio Santoro[h], Riccardo Basosi[a], Nicolas Ferré[i], and Massimo Olivucci[a,c,1]

[a]Dipartimento di Chimica, Università di Siena, via Aldo Moro 2, I-53100 Siena, Italy; [c]Chemistry Department, Bowling Green State University, Bowling Green, OH 43403; [b]Departamento de Ingeniería Química y Química Física, Universidad de Extremadura, Avenida de Elvas s/n 06071 Badajoz, Spain; [d]Physikalisch-Chemisches Institut, Universität Zürich, Winterthurerstrasse 190, 8057 Zürich, Switzerland; [e]Institut de Physique et Chimie des Matériaux de Strasbourg–Group of Nonlinear Optics, Unité Mixte de la Recherche 7504, Centre National de la Recherche Scientifique, Université Louis Pasteur, 23 Rue du Loess, 67034 Strasbourg Cédex, France; [f]Laboratoire de Spectroscopie Ultrarapide, Ecole Polytechnique Fédérale de Lausanne, CH-1015 Lausanne-Dorigny, Switzerland; [g]Dipartimento di Scienze Farmaceutiche, Università di Ferrara, via Fossato di Mortara 17-19, I-44100 Ferrara, Italy; [h]Istituto per i Processi Chimico-Fisici del Consiglio Nazionale delle Ricerche, Via Moruzzi 1, I-56124 Pisa, Italy; and [i]Laboratoire de Chimie Théorique et de Modélisation Moléculaire, Unité Mixte de la Recherche 6517, Centre National de la Recherche Scientifique Université de Provence, Case 521–Faculté de Saint-Jérôme, Av. Esc. Normandie Niemen, 13397 Marseille Cedex 20, France

Edited by Josef Michl, University of Colorado, Boulder, CO, and approved September 16, 2008 (received for review March 10, 2008)

Single molecules that act as light-energy transducers (e.g., converting the energy of a photon into atomic-level mechanical motion) are examples of minimal molecular devices. Here, we focus on a molecular switch designed by merging a conformationally locked diarylidene skeleton with a retinal-like Schiff base and capable of mimicking, in solution, different aspects of the transduction of the visual pigment Rhodopsin. Complementary ab initio multiconfigurational quantum chemistry-based computations and time-resolved spectroscopy are used to follow the light-induced isomerization of the switch in methanol. The results show that, similar to rhodopsin, the isomerization occurs on a 0.3-ps time scale and is followed by <10-ps cooling and solvation. The entire (2-photon-powered) switch cycle was traced by following the evolution of its infrared spectrum. These measurements indicate that a full cycle can be completed within 20 ps.

CASPT2//CASSCF | mid-IR | photochemical switch | time resolved spectroscopy | UV-vis

Molecular switches based on photochemical *E*/*Z* isomerizations have been used in different contexts to convert light energy into "mechanical" motion at the molecular level (1–3). For instance, switches based on azobenzene have been used to control ion complexation (4, 5), electronic properties (6), catalysis (7), and the folding of peptides (8–13) whereas diarylidenes have provided the framework for the construction of rotary motors and transmissions (14). The computer modeling of switches that differ in size, polarity, and isomerization mechanism represents an attractive research target (15) yielding building blocks to be used in diverse molecular environments. However, this cannot be limited to the computation of equilibrium properties but requires the description of the entire photocycle. In other words, one needs to compute the potential energy surfaces controlling the switch E $\rightarrow$ Z and Z $\rightarrow$ E excited-state evolution, its decay and ground state relaxation, and the competing thermal *E*/*Z* isomerization in the proper environment (e.g., in solution or in a biomolecule backbone). The complexity of these calculations impedes the study of candidates that are intractable with accurate quantum chemical methods (allowing comparison with spectroscopic data) or that feature, as for azobenzene and diarylidenes (16), more than 1 low-lying excited state, leading to a plethora of reaction paths to be computed.

The retinal protonated Schiff-base chromophore of rhodopsins (17–19) constitutes an example of an *E*/*Z* switch shaped by biological evolution that can be modeled with quantitative computations (20). In bovine rhodopsin (Rh), a selective photoisomerization of the 11-*cis* chromophore (PSB11) occurs via evolution of a single $\pi \rightarrow \pi^*$ excited state (S_1) that survives for only 150 fs and yields, upon decay, the *all-trans* ground state (S_0) product with a 67% quantum yield (16, 20). Although these properties make Rh an excellent reference for the design of *E*/*Z* switches, irradiation of PSB11 in solution (26, 27) features an unselective isomerization and a picosecond excited-state lifetime (18) prompting a search for artificial Rh-mimetic molecules. To address this problem, we have shown (21) that, in methanol solution, the *N*-alkylated indanylidene-pyrroline Schiff base (NAIP) **1** displays excited-state properties similar to those of Rh-embedded PSB11. We have also shown that NAIPs can be prepared in good yields (>80%) through a cyclopropyl ring-opening/nitrilium ring-closing tandem reaction (22).

In the present report, complementary computational and experimental tools are used to characterize the photoisomerization of **1**. We show that quantum-mechanics/molecular-mechanics (QM/MM) calculations based on ab initio (i.e., first-principle) multiconfigurational second-order perturbation theory (CASPT2), and complete-active-space self-consistent-field (CASSCF) quantum chemical methods point to E-**1** $\rightarrow$ Z-**1** and Z-**1** $\rightarrow$ E-**1** S_1 isomerization paths that intercept distinct conical intersections on a 200-fs time scale. Such features are probed via time-resolved UV-vis absorption, emission, and mid-IR spectroscopy and show that the Z $\rightarrow$ E $\rightarrow$ Z photocycle (*Inset* in Fig. 1) is completed in picoseconds.

Results and Discussion

Reaction Path Computation and Analysis. In Fig. 1, we report the CASPT2//CASSCF/AMBER photochemical reaction paths (a combination of a $\pi \rightarrow \pi^*$ S_1 reaction path followed by a S_0 relaxation path) for the chloride·Z-**1** (left) and chloride·E-**1** (right) ion pairs (from now on Z-**1** and E-**1,** respectively) in methanol solution. The relative stability of Z-**1** and E-**1** has been determined in terms of the difference in Gibbs free energy between the solvated ion pairs by using averaged solvent electrostatic potential/molecular dynamics (ASEP/MD) computations (23). [see supporting information (SI) *Appendix*]. The

Author contributions: J.H., S.H., and M.O. designed research; A.S., E.M., M.R., J.B., D.S., J.L., A.C., and F.S. performed research; V.Z., S.F., R.B., and N.F. contributed new reagents/analytic tools; A.S., E.M., J.H., J.B., D.S., J.L., S.H., A.C., M.C., F.S., and M.O. analyzed data; and J.H., S.H., and M.O. wrote the paper.

The authors declare no conflict of interest.

This article is a PNAS Direct Submission.

[1]To whom correspondence may be addressed. E-mail: olivucci@unisi.it, stefan.haacke@ipcms.u-strasbg.fr, or j.helbing@pci.uzh.ch.

This article contains supporting information online at www.pnas.org/cgi/content/full/0802376105/DCSupplemental.

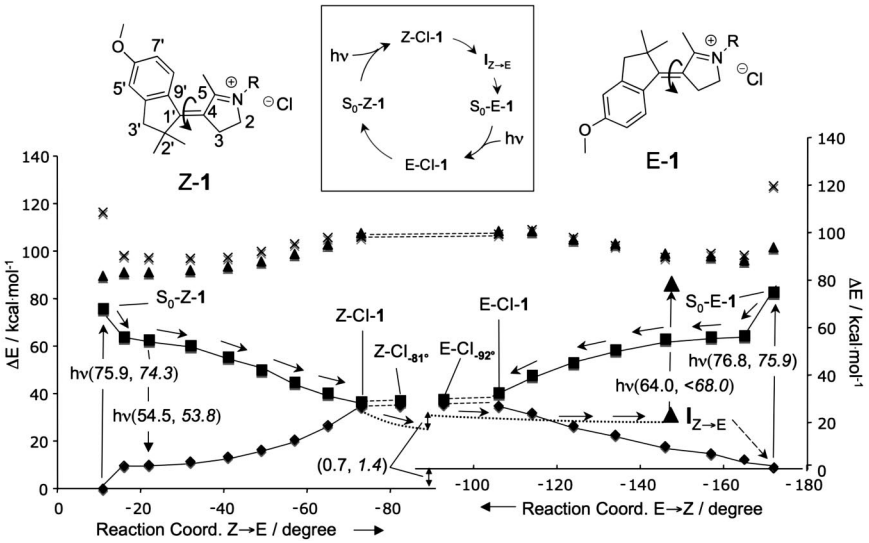

Fig. 1. Excited-state reaction paths. (*Inset*) Overview of the studied parts of the photocycle. CASPT2//CASSCF/6–31G*/AMBER S_0 (diamonds), S_1 (squares), S_2 (triangles), and S_3 (crosses) energy profiles along the photoisomerization coordinate (the dihedral angle C_5–C_4–$C_{1'}$–$C_{9'}$) of Z-1 and E-1. Notice that the protonated (R═H) rather then methylated (R═Me) derivative is used for all computations. S_0–Z–1 and S_0–E–1 correspond to the S_0 equilibrium structure. The Z–CI–1, $Z\text{–CI}_{-81°}$, E—CI–1, and $E\text{–CI}_{92°}$ correspond to conical intersection structures. (The Z and E conical intersections have different solute and solvent shell structures). $I_{Z\to E}$ corresponds to an intermediate generated via a relaxation starting at Z–CI–1 with a fixed solvent shell (dotted lines, see details in Fig. 2*B*). The corresponding S_0 path starting at E–CI–1 has also been computed (data not shown) but leads to a structure close to S_0–Z–1 (see *SI Appendix*). The stream of arrows departing from S_0–Z–1 and ending at $I_{Z\to E}$ indicates the computed Z → E photochemical reaction path. The dashed arrow on the bottom right indicates that relaxation of the $I_{Z\to E}$ solvent shell produces E-1. The vertical arrows indicate the electronic transition (absorption and fluorescence) probed experimentally. The double arrow indicates the S_0 Gibbs free-energy difference of S_0–Z–1 and S_0–E–1. The computed and observed (italics) energies are given in parentheses. The S_0–Z–1 and S_0–E–1 observed excitation energies are from ref. 21.

results indicate that, at 298 K, E-**1** is 0.7 kcal·mol^{-1} higher in free energy than Z-**1**. This value compares well with the 1.4 kcal·mol^{-1} free-energy difference (Z/E ratio is 92:8) derived from HPLC analysis of the thermally equilibrated mixture.

From inspection of Fig. 1, it is apparent that the $S_0 \to S_1$ photoexcitation of Z-**1** and E-**1** releases these systems along barrierless paths that evolve toward 2 distinct Z-CI-**1** and E-CI-**1** conical intersections. As found for PSB11 in Rh, these paths span a single excited-state energy surface with a charge transfer character (i.e., the —C═N— positive charge translocates toward the phenyl group) that increases moving from the Franck–Condon region to the intersections. The existence of the additional intersection points $Z\text{-CI}_{-81°}$ and $E\text{-CI}_{-92°}$ indicates that Z-CI-**1** and E-CI-**1** are part of a smooth intersection space segment spanning the bottom of the S_1 energy surface and providing prompt access to the S_0 energy surface.

Fig. 2*A* reports the values of the computed oscillator strength (**f**) along the $Z \to E$ path for the transition between S_0 and the first three excited singlet states. Such data indicate a prompt and intense $S_1 \to S_0$ emission in the −17° to −20° region of the path. This emission (λ^{f}_{max} ≈530 nm, see the 54.5 kcal·mol^{-1} S_1-S_0 energy differences in Fig. 1) must arise immediately after photoexcitation and shift to the red as a function of time.

In Fig. 2*B*, we report the energy profile along the S_0 relaxation path departing from Z-CI-**1** and pointing toward the E-**1** photoproduct. The path (we use a fixed solvent shell to model the initial relaxation where the solute structure changes faster than solvent reorientation) leads to a flat region of the S_0 energy surface centered on an approximately −150° twisted structure ($\mathbf{I}_{Z\to E}$). However, upon relaxation of the solvent, $\mathbf{I}_{Z\to E}$ further relaxes to an approximately −180° twisted minimum corresponding to S_0-E-**1**. In fact, a limited pyrroline out-of-plane distortion allows for a path where the distance between the methyl groups at $C_{2'}$ and C_5 is large enough to avoid steric clash. To estimate the excited state lifetime of Z-**1**, we take advantage of the $Z \to E$ reaction path data. Analysis of the S_1 reaction coordinate indicates that there are 2 modes driving the reaction. The stretching mode corresponds to the expansion of the double bonds and contraction of the single bonds. The torsional mode is the reactive mode and describes the twisting of the central double bond. We assume that a 2-dimensional potential-energy surface suffices to describe the S_1 population dynamics. Accordingly, we have fitted a suitable function of the $C_{1'}$–C_4 bond length and $C_{9'}$–$C_{1'}$–C_4–C_5 twist (see *SI Appendix*) against the $Z \to E$ data of Fig. 1. As shown in Fig. 2*C*, the resulting (effective) potential energy surface incorporates the S_1 CASPT2//CASSCF/AMBER $Z \to E$ energy profile. The S_1 population motion is simulated generating a "classical" wave packet of 1,000 trajectories defined by constructing a Wigner distribution (see *Materials and Methods*). We find that the population oscillates across the reaction-path valley and broadens but does not split. The population maximum (i.e., the average trajectory) reaches the energy minimum associated with the Z-CI-**1** decay point on a 200-fs time scale pointing to a subpicosecond lifetime for S_1.

The model above predicts (see *SI Appendix*) that the stretching mode is immediately excited and, provided little kinetic energy redistribution occurs, it maintains ≈5 kcal·mol^{-1} of kinetic energy for the rest of the S_1 evolution. In contrast, the isomerization mode accelerates slowly until ≈100 fs but then quickly incorporates kinetic energy reaching a >25 kcal·mol^{-1} value upon $S_1 \to S_0$ decay at ≈200-fs delay. This type of behavior has also been found for Rh (24), where the kinetic energy evolution of its PSB11 chromophore was determined by computing scaled-CASSCF/AMBER trajectories of a molecular model of the entire pigment.

Time-Resolved UV-Vis Spectroscopy. Fig. 3*A* shows the time-resolved emission data of Z-**1**. The fluorescence excited via the $S_0 \to S_1$ transition at 400 nm rises instantaneously and covers most of the visible spectral region. It shows a blue-centered band at time zero that red-shifts and disappears in <1 ps. The fitting of the kinetics traces (see *SI Appendix*) with exponential func-

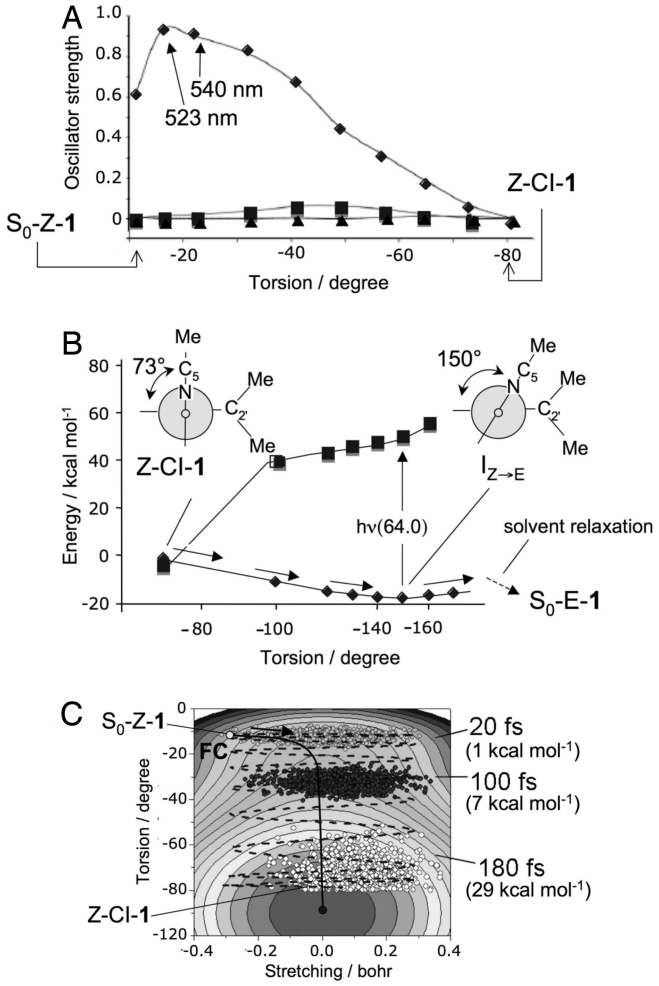

Fig. 2. Analysis of the Z → E photochemical reaction path. (*A*) Change in CASSCF/6–31G*/AMBER $S_0 \rightarrow S_1$ (diamonds), $S_0 \rightarrow S_2$ (triangles), and $S_0 \rightarrow S_3$ (squares) oscillator strengths. (*B*) CASPT2//CASSCF/6–31G*/AMBER S_0 (diamonds), S_1 (squares) energy profiles along the Z → E S_0 relaxation path computed with a fixed solvent shell and starting at Z–Cl–1. (*C*) Simulation of the population dynamics along a 2D-model of the S_1 energy surface. The arrow indicates the initial direction of the gradient. The values in parentheses refer to the kinetic-energy component along the torsion (i.e., isomerization) mode.

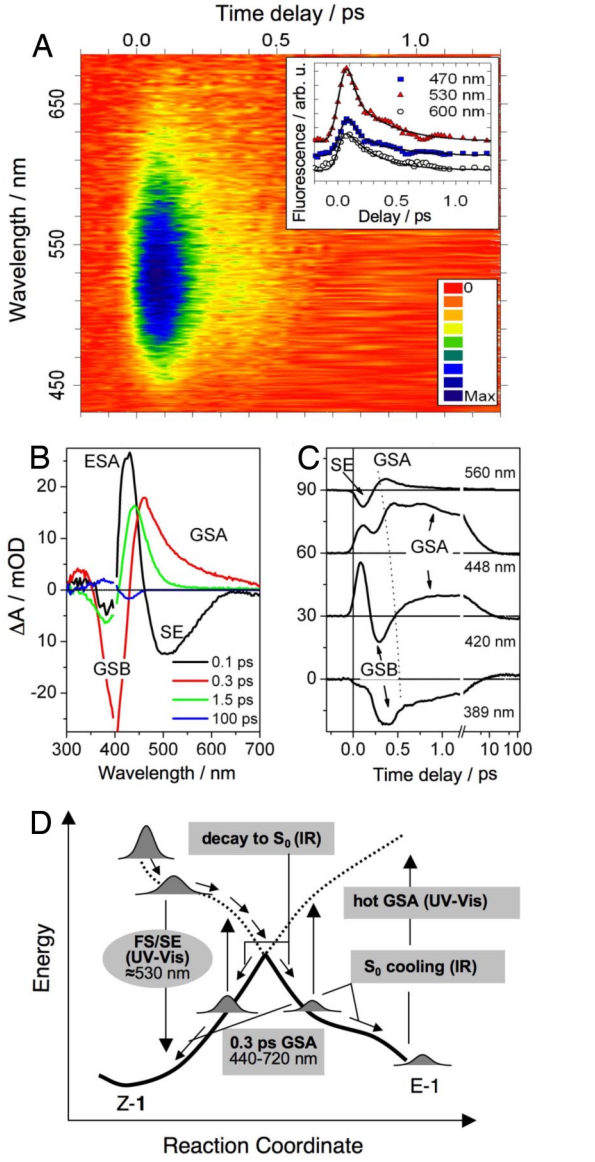

Fig. 3. Ultrafast UV-vis spectroscopy. (*A*) Time- and wavelength-resolved fluorescence of Z-1 with color-scale-coded intensity. The maximum at 520–530 nm and a biphasic decay are apparent. (*Inset*) Kinetic traces at selected wavelengths (data points are vertically shifted for the sake of clarity). Solid lines are best-fits to the data. (*B*) Time-resolved absorption spectra (change in absorbance, ΔA), showing $S_1 \rightarrow S_n$ absorption (ESA, 425 and 330 nm), $S_1 \rightarrow S_0$ stimulated emission (SE, 460–700 nm) and the S_0 absorption (GSA, 440–700 nm), blue-shifting at later times (420–480 nm). The 100-ps data are the E-Z difference spectrum. Data points with residual pump light scatter (395–405 nm) are removed. (*C*) Selected kinetic traces, vertically shifted by 30 mOD. The dashed line is a guide to the eye highlighting the blue-shifting early GSA feature (*D*) Schematic view of the observed spectral transitions on the S_0 (solid lines) and S_1 (dashed lines) potential-energy surfaces as a function of the (Z → E) reaction coordinate. Arrows indicate the course of the reaction as suggested by the observed sequence ESA/FS/SE → GSA → hot-GSA. GSA and hot-GSA arise, most probably, from both Z and E conformers. The phases of the photoreaction probed by time-resolved IR spectroscopy are also indicated.

tions convoluted with the instrument response function (solid lines) reveals a biphasic behavior at wavelengths <600 nm [time constants $\tau_1 < 40$ fs (i.e., an instrumental reponse-limited decay) and $\tau_2 = 300 \pm 30$ fs] and a single-exponential decay with τ_2 at wavelengths >600 nm]. This fluorescence is assigned to the $S_1 \rightarrow S_0$ transition because: (*i*) it lies at the red of the singlet absorption band, (*ii*) appears promptly, and (*iii*) at early times is centered at 530 nm (53.8 kcal·mol^{-1}), consistent with the S_1–S_0 energy gap and **f** values for approximately −20° torsions. The observed dynamics is consistent with the S_1 $Z \rightarrow E$ reaction path of Fig. 1 and modeled ≈200-fs decay. The initial relaxation from the Franck–Condon (S_0-Z-**1**) window along the stretching mode is probably reflected by the τ_1 component, whereas the slower torsional motion, which depopulates the small-angle fluorescent window with high oscillator strength gives rise to the slower τ_2 component.

We show transient absorption spectra (Fig. 3*B*) and kinetic traces (Fig. 3*C*) after Z-**1** excitation at 400 nm. The first 200 fs are dominated by the S_1 dynamics and later times by the S_0 relaxation, leading ultimately to relaxed E-**1** and Z-**1** conformations. This equilibrium situation is reached for $t > 30$ ps, and is best borne out by the *Z*/*E* difference spectrum at 100 ps. In the spectrum recorded after 0.1 ps, a broad stimulated emission (SE) band is observed at ≈500–520 nm (55 kcal·mol^{-1}), as expected from the above fluorescence. In addition, we detect excited state absorption (ESA) at ≈430 nm (66.3 kcal·mol^{-1}). Because the computed $S_1 \rightarrow S_3$ transition has a negligible **f** value along the

path (Fig. 2*A*), such signal is assigned to a $S_1 \rightarrow S_n$ transition. The negative signal in the 360- to 390-nm range is due to removal of molecules from S_0 (ground-state bleach, GSB). Fitting of the ESA and SE kinetic traces at 420 and 560 nm, respectively, yields a sub-100-fs decay time that parallels the fast τ_1 relaxation time retrieved from the fluorescence decay.

The SE does not show the τ_2 component of the fluorescence, because, on this time scale, the data are dominated by a broad S_0 absorption signal (GSA). The GSA is clearly visible in the 0.3-ps spectrum and gives rise to a sharp feature in the kinetic traces (>420 nm). It has a delayed onset (≈220 fs with respect to the excitation pulse) and decays with $\tau_3 = 200 \pm 40$ fs. [Fitting the GSA without a delayed onset yields unsatisfactory results. At 540 nm, we find that this delay time is 180 ± 20 fs. It shifts to later times as one goes from 580 to 440 nm (Fig. 3*C*)]. Because the model of Fig. 2*C* and the fluorescence data indicate S_1 decay occurring on the same or even faster time scales, we suggest that the GSA is associated with a repopulation of S_0 after decay at the conical intersection Z–CI–**1**. The small-amplitude long-wavelength wing (600–720 nm) of this band (0.3-ps spectrum in Fig. 3*B*) would represent molecules with larger twist angles. The wavelength-dependent onset time is consistent with a wave-packet-like evolution triggered by decay at Z—CI–**1**, with the 180- to 250-fs onset delay giving an approximate value for the internal conversion time. Although the GSA is most probably dominated by vibrationally hot Z-**1**, torsionnally unrelaxed E-**1** products (tentatively associated with the computed 445-nm absorbing $I_{Z \rightarrow E}$ structure) are simultaneously formed at the Z–CI–**1** bifurcation. The isomerization time is thus ≈200 fs, i.e., close to the 180-fs time observed for the production of photorhodopsin: the primary and nonisolable S_0 intermediate of Rh (17).

At times >1 ps, the GSA signal is blue-shifted and is limited to wavelengths <500 nm, being attributed to vibrationally excited E-**1** or Z-**1**. The average decay time of the spectrally integrated signal of this "hot" S_0 absorption (GSA) is ≈5 ps, as expected for vibrational-energy relaxation in methanol and in agreement with the mid-IR results (see below). Fits of the GSB recovery ≈ 380 nm yield a fast ≈200-fs time and a slower ≈5-ps component. The latter is the counterpart of the GSA decay due to vibrational relaxation, whereas the former reflects the S_0 recovery in both Z and E forms (isomerization). For delay times >25 ps, a quasistationary spectrum is observed (100-ps spectrum, Fig. 3*B*) that displays the bleach of Z-**1** (428 nm) and absorption due to the E isomers (380 nm). The signal level is consistent with the reported (21) 0.20 Z → E isomerization quantum yield.

In Fig. 3*D*, we summarize the relationship between the signals discussed above and the computed reaction path. The early sub-100-fs parts of fluorescence, SE (and ESA) are assigned to molecules with a twisting angle of less than −30°, located in the region of highest S_1-S_0 **f** value. This is corroborated by the agreement of the calculated and observed emission energies (Fig. 1). Progression toward the conical intersection is predicted to occur on a ≈90-fs time scale in accord with the τ_1 decay time, but molecules with smaller kinetic energies populate larger twist angles (with lower S_1-S_0 **f** values) and show the weaker red-shifted fluorescence decaying with a $\tau_2 = 300$ fs. The early τ_1 decay of S_1 triggers the fast-appearing GSA that dominates the long-wavelength transients at 0.3 ps. This early GSA is associated with highly twisted Z- and E-like molecules. This assignment is rationalized by the calculations predicting a transition energy of 40 kcal·mol^{-1} (715 nm) for approximately −40° and approximately −140° twisting angles. S_0 cooling then leads to nearly equilibrated Z and E structures on a ≈5-ps time scale.

Time-Resolved Mid-IR Spectroscopy. UV-pump-mid-IR-probe spectra were recorded in the 1,450- to 1,650-cm^{-1} region, where

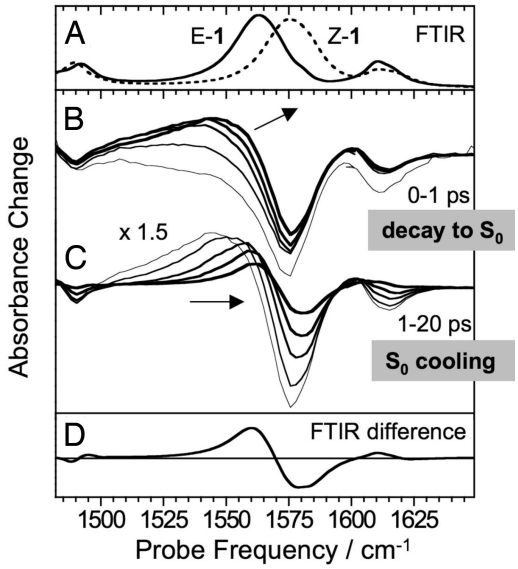

Fig. 4. Time-resolved mid-IR spectra. (*A*) FTIR absorption spectra of Z-1 (dashed line) and E-1 (solid line). (*B*) Transient spectra at different delays (0, 0.2, 0.4, 0.6, and 1 ps) after the excitation of Z-1 at 420 nm. (*C*) Transient spectra at delays 1, 2, 5, 10, and 20 ps, all scaled by a factor of 1.5 for better visibility. (*D*) Difference between the FTIR spectra shown in *A* reproducing the transient spectra at delays >30 ps.

the $C_{1'}$–C_4 stretch band of Z-**1** at 1,575 cm^{-1} is spectrally isolated from the E-**1** band (Fig. 4*A*). A smaller band at 1,610 cm^{-1} can be assigned to the N–C_5 stretch mode based upon vibrational frequency calculations (21). Immediately after Z-**1** excitation, a bleach spectrum is observed that is a replica of the absorption spectrum (Fig. 4*B*), in line with the expectation that the $C_{1'}$–C_4 stretch should disappear from S_1 because of the loss of double bond character. Within 1 ps, a broad band grows in at the lower-frequency side of the original spectrum. This band continuously narrows and shifts to higher frequencies, overlapping with the original negative bleach (Fig. 4*C*). After 30 ps, the spectrum is stable and closely resembles the steady-state E-Z difference spectrum, recorded after continuous 435-nm irradiation in a FTIR spectrometer (Fig. 4*D*).

Growth and shift of the photoproduct band become more evident after subtracting from all subsequent signals the transient absorption spectrum at zero time delay (*SI Appendix*). This reveals that the integrated intensity of the $C_{1'}$–C_4 stretch is almost completely recovered on a time scale of a few hundred femtoseconds in agreement with the fluorescence decay time and consistent with the fact that the double-bond character is restored on S_0. Thus, the induced absorption signal is assigned to S_0 species (Fig. 3*D*). Because of the S_1 population branching occurring upon decay at Z–CI–**1**, both molecules relaxing to E-**1** and molecules returning to Z-**1** contribute to the signal. Indeed, 1 ps after photoexcitation, the excess energy from the S_1-S_0 decay results in a nonequilibrium excitation of low-frequency vibrational modes, which anharmonically couple to the $C_{1'}$–C_4 stretch, leading to a red-shift and spectral broadening (9). The steady-state difference spectrum is observed only after dissipation of this excess energy to the solvent. A moment analysis of the pump-probe data shows that, next to a small subpicosecond component, the main shift of the photoproduct band takes place on a 6- to 9-ps time scale, when only very small changes in the integrated band intensity are observed. This cooling/solvation time scale is in good agreement with the spectral dynamics observed for the UV-vis GSA signal. The quantum yield of the Z → E isomerization was calculated by comparing the magni-

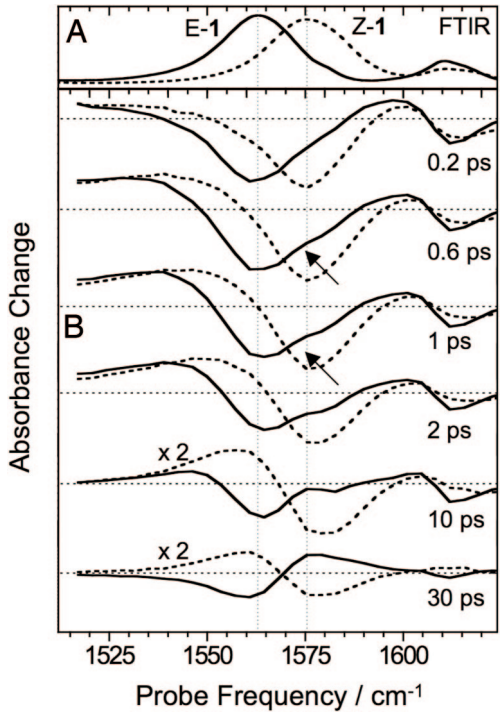

Fig. 5. Ultrafast bidirectional isomerization: (*A*) FTIR absorption spectra of Z-1 (dashed line) and E-1 (solid line). (*B*) Transient mid-IR spectra at different delays after the excitation of Z-1 (dashed line) and E-1 (solid line) at 388 nm.

tudes of initial bleach and final difference spectrum (*SI Appendix*) to the calibrated FTIR absorption and difference absorption spectra (25) yielding 0.21 ± 0.03. This is consistent with steady-state HPLC measurements (21).

The reverse E → Z photoreaction [occurring with a 0.35 quantum yield (21)] was followed after transferring 87% of all molecules to the E form by continuous irradiation at 454.5 nm. By setting the UV-pump-laser wavelength at 388 nm, where the E-**1** absorption is 30% stronger than the Z-**1** absorption, we made sure that at least 90% of the photoexcited molecules were initially in the E form. In Fig. 5 we compare the transient spectra for E-**1** to those for Z-**1** under identical conditions. The spectral changes in both isomerization directions occur in parallel. In particular, the growth of the photoproduct spectrum and its shift on a <10-ps time scale are observed in both cases consistently with the barrierless paths of Fig. 1. However, for E-**1,** the spectral shift due to the isomerization is of opposite direction with respect to the initial (heat-induced) red-shift, and the isomerization process can be better distinguished. Indeed, a small shoulder at the spectral position of the Z-**1** band can be seen in the transient spectra already 0.5–1 ps after E-**1** photoexcitation (see arrows in Fig. 5), confirming the ultrafast formation of Z-**1**. The sharpening and increase of this feature beyond 1 ps is again related to the vibrational relaxation of the S_0 species.

Conclusions

The development of single-molecule *E*/*Z* switches and rotary motors (chiral switches that undergo consecutive unidirectional Z → E or E → Z photoisomerizations) would require building blocks featuring faster response times and higher quantum yields. Studying the properties of a series of biarylidene motors, Feringa and coworkers (14) have unveiled the complexity of the response time concept whose value may span 1 or more orders of magnitude as a function of framework and substitution pattern. In these systems, the isomerization time scale is set by a conformational helix inversion (e.g., from a P to a M helix) of either the Z or E form of the molecule:

$$Z(M) \xrightarrow{h\nu} E(P) \xrightarrow{\Delta} E(M) \xrightarrow{h\nu} Z(P) \xrightarrow{\Delta} Z(M).$$

The first and third steps are photoisomerizations, whereas the second and fourth steps are slow (rate-limiting) thermal helix inversions. The slow inversion steps are required to generate a conformer allowing for a forward, rather than reverse, subsequent photoreaction.

NAIPs are "chimerical" switches that incorporate into the Feringa's biarylidenes skeleton a protonated or alkylated Schiff base function. Although the application of NAIPs to the construction of rotary motors will require further research work, our computational and spectroscopic data indicate that their photoinduced dynamics replicates the dynamics of the PSB11 isomerization in Rh. This protein features a S_1 lifetime of ≈150 fs, a S_0 transient (photorodopsin) appearance time of 180 fs, and a primary photoproduct (bathorhodopsin) appearance time of ≈6 ps. These time scales match the observed and computed 0.1- to 0.3-ps S_1 lifetime of Z-**1**, the 200- to 250-fs S_0 replenishment, and the 6- to 9-ps time scale for the E-**1** photoproduct cooling/solvation. Such properties suggest that NAIP-based motors may complete a half-rotary cycle in <10 ps, i.e., a few orders-of-magnitude faster than the fastest (≈6 μs for half-cycle) known biarylidene (26).

The replacement of the slow biarylidene helix inversion step with an impulsive reaction shuttling the primary photoproduct population (e.g., E(P) and Z(P) in the cycle) toward the stable conformers (e.g., E(M) and Z(M), respectively) may lead to much faster light-powered rotary motors. However, this can be implemented only in switches where an ultrafast photochemical reaction produces a product with a nonstatistical distribution of the vibrational energy polarized on the reactive (Z → E or E → Z) mode. It is likely that, after insertion of a stereogenic center in position 2, 3, or 2′ [the synthetic routes do not exclude such possibility (22)], NAIP switches could provide this type of system. In fact, as shown above, upon decay from S_1, > 25 kcal·mol^{-1} of kinetic energy are predicted to be located on the isomerization mode. Such momentum, together with the additional torque provided by the following S_0 reconstitution of the central double bond, may push part of the population well beyond the initial conformation, vibrational relaxation completing the process within 10 ps.

Despite the fact that the excited-state populations of **1** and Rh both evolve along a single path intercepting a conical intersection, the corresponding reaction coordinates indicate different isomerization mechanisms. Indeed, the S_1 evolution of PSB11 in Rh occurs via an "asynchronous crankshaft" mode involving twisting of 2 adjacent double bonds (26). Because of its locked skeleton, such motion cannot be accomplished in **1** that isomerizes by twisting a single double bond. This difference is accompanied by a lower value of the kinetic energy deposited, upon decay to S_0, in the reactive modes that is <10 kcal·mol^{-1} in Rh, in contrast to the above 25 kcal·mol^{-1} for **1**. It is also important to point out that, relative to **1**, the photoisomerization quantum yield of Rh is 2 to 3 times larger. These facts suggest that NAIPs not only provide a route to new materials but that they also constitute attractive systems for the investigation of fundamental problems such as the relationship between excited-state evolution and quantum yields.

Materials and Methods

Computations. The ab initio CASSCF method (27) is a multiconfigurational quantum chemical method providing the 0th-order wave function for subsequent CASPT2 (28) computations leading to a quantitative evaluation of

electronic energies. The ab initio CASPT2//CASSCF protocol (where geometries and electronic energies are determined at the CASSCF and CASPT2 levels, respectively, with an active space comprising the full 12-electron in 11-orbital π-system of **1**) has been recently implemented in a QM/MM scheme (20, 29) allowing for the evaluation of the excitation energies and barriers of chromophores (treated quantum mechanically) embedded in explicit solution or protein environments (described by the AMBER force field). The quality of the used CASPT2//CASSCF/AMBER methanol solution model (that uses a single solvent shell approximation. See *SI Appendix*) is probed by computing the Z-**1** (21) and E-**1** $S_0 \rightarrow S_1$, $S_0 \rightarrow S_2$, and $S_0 \rightarrow S_3$ vertical excitation energies. These values reproduce the observed quantities with a $<$3-kcal·mol^{-1} error (Fig. 1), and the corresponding **f** values reproduce the observed transition intensity patterns. These data are confirmed via ASEP/MD computations (23) that, via a self-consistent protocol, yield a congruous description of the solvent shells of the associated average electrostatic fields and of the Z-**1** and E-**1** equilibrium structures. The ASEP/MD Z-**1** and E-**1** S_0 equilibrium structures differ from the one computed with the approximate solvent model of 0.030 and 0.019 Å, respectively (RMS deviation). Similarly, the 2 sets of excitation energies differ by -0.1 and 2.2 kcal·mol^{-1} for the Z-**1** and E-**1** isomers, respectively.

The S_1 reaction coordinates of Fig. 1 are computed via unconstrained geometry optimizations starting at S_0–Z–**1** and S_0–E–**1** and yielding 2 S_1 relaxed structures. From these structures, a relaxed scan along the $C_{9'}$–$C_{1'}$–C_4–C_5 angle is computed with steps of $-10°$ (for Z-**1**) or $+10°$ (for E-**1**). This protocol [based on a scan rather than an Intrinsic Reaction Coordinate (IRC) calculation] avoids problems associated with the flatness of the energy surface. Its validity has been assessed for Z-**1** by computing the initial part of the IRC. The IRC path (see *SI Appendix*) intercepts the optimized S_1 point at $-17°$ twisting and then continues along the points of the scan indicating that the presented paths provides a mechanistically valid approximations of minimum energy paths. The S_1 paths computed with a frozen or a relaxed solvent shell (with respect with the initial S_0–Z–**1** shell) show only small differences (see *SI Appendix*).

Ultrafast UV-Vis and UV-Mid-IR Spectroscopy. Z-**1**, prepared as described in ref. 22, was dissolved in methanol-d4 dried over molecular sieves for the IR experiments and in spectroscopy grade MeOH for the UV-vis pump-probe experiments. Solutions of ≈10 mmol/L were used for time-resolved IR spectroscopy in a 100-μm-thick flow cell (OD 0.8–1.2 at the $S_0 \rightarrow S_1$ absorption maximum at 390 nm). More-diluted samples were used for the UV-Vis pump-probe and fluorescence experiments performed in 0.5-mm path-length flow cells (OD ≈0.5). Thermal relaxation from the E to the Z forms takes place with a 17.5-h time constant at room temperature. Therefore, to minimize E-**1** accumulation during the measurements (typically 1–2 h for a complete dataset), a sufficiently large amount of sample was circulated in a flow cell at a rate high enough to exchange the sample after each laser shot. Sub-100-fs pulses at 388–420 nm were obtained by frequency-doubling the output of commercial Ti:Sapphire laser systems and used to excite $<$5% of the molecules in the laser focus. Home-built setups were used for femtosecond fluorescence upconversion (30), UV-vis, and UV-mid-IR pump-probe measurements. The temporal resolution was 80–120 fs in the former 2 experiments and 300 fs in the latter (see *SI Appendix*).

ACKNOWLEDGMENTS. M.O. is grateful to Bowling Green State University for a start-up grant. This work was partially supported by the Università di Siena (Progetto di Ateneo 05/07), Fondazione Monte dei Paschi and Research Programmes of National Interest (PRIN) 2006. We thank the Ohio Supercomputer Center for granted calculation time. S.H. acknowledges start-up funds from the Conseil Scientifique de l'Université Louis Pasteur, from the Centre National de la Recherche Scientifique, and from the Institut de Physique et Chimie des Matériaux de Strasbourg (''program mi-lourd 2005'').

1. Sauvage J-P (2001) *Molecular Machines and Motors* (Springer, Heidelberg).
2. Drexler K-E (1992) *Nanosystems: Molecular Machinery, Manufacturing and Computation* (Wiley, New York).
3. Balzani V, Credi A, Venturi M (2003) *Molecular Devices and Machines. A Journey into the Nanoworld* (Wiley-VCH, Weinheim, Germany).
4. Shinkai S, *et al.* (1980) Photoresponsive crown ethers. 1. *Cis–trans* isomerism of azabenzene as a tool to enforce conformational changes of crown ethers and polymers. *J Am Chem Soc* 102:5860–5865.
5. Shinkai S, Minami T, Kusano Y, Manabe O (1983) Photoresponsive crown ethers. 8. Azobenzenophane-type ''switched-on'' crown ethers which exhibit an all-or-nothing change in ion-binding ability. *J Am Chem Soc* 105:1851–1856.
6. Jousselme B, *et al.* (2003) Photomechanical actuation and manipulation of the electronic properties of linear p-conjugated systems. *J Am Chem Soc* 125:2888–2889.
7. Cacciapaglia R, Stefano SD, Mandolini L (2003) The bis-barium complex of a butterfly crown ether as a phototunable supramolecular catalyst. *J Am Chem Soc* 125:2224–2227.
8. Behrendt R, *et al.* (1999) Photomodulation of the conformation of cyclic peptides with azobenzene moieties in the peptide backbone. *Angew Chem Int Ed* 38:2771–2774.
9. Bredenbeck J, *et al.* (2003) Picosecond conformational transition and equilibration of a cyclic peptide. *Proc Natl Acad Sci USA* 100:6452–6457.
10. Ulysse L, Cubillos J, Chmielewski J (1995) Photoregulation of cyclic peptide conformation. *J Am Chem Soc* 117:8466–8467.
11. Rudolph-Böhner S, *et al.* (1997) Photomodulation of conformational states of p-phenylazobenzyloxycarbonyl-L-proline and related peptides. *J Photochem Photobiol A* 105:235–248.
12. Renner C, Behrendt R, Spörlein S, Wachtveitl J, Moroder L (2000) Photomodulation of conformational states. I. Mono- and bicyclic peptides with (4-amino)phenylazobenzoic acid as backbone constituent. *Biopolymers* 54:489–500.
13. Spörlein S, *et al.* (2002) Ultrafast spectroscopy reveals subnanosecond peptide conformational dynamics and validates molecular dynamics simulation. *Proc Natl Acad Sci USA* 99:7998–8002.
14. Feringa BL (2007) The art of building small: From molecular switches to molecular motors. *J Org Chem* 72:6635–6652.
15. Martinez TJ (2006) Insights for light-driven molecular devices from ab initio multiple spawning excited-state dynamics of organic and biological chromophores. *Acc Chem Res* 39:119–126.
16. Schuddeboom W, *et al.* (1993) Sudden polarization in the twisted, phantom state of tetraphenylethylene detected by time-resolved microwave conductivity. *J Am Chem Soc* 115:3286–3289.
17. Mathies RA, Lugtenburg J (2000) in *Handbook of Biological Physics*, eds Stavenga DG, de Grip WJ, Pugh EN (Elsevier, Amsterdam), pp 55–90.
18. Kandori H, Shichida Y, Yoshizawa T (2001) Photoisomerization in rhodopsin. *Biochemistry (Moscow)* 66:1483–1498.
19. Teller DC, Okada T, Behnke CA, Palczewski K, Stenkamp RE (2001) Advances in determination of high-resolution three-dimensional structure of rhodopsin, a model of G-protein-coupled receptors (GPCRs). *Biochemistry* 40:7761–7772.
20. Andruniow T, Ferré N, Olivucci M (2004) Structure, initial excited-state relaxation, and energy storage of rhodopsin resolved at the multiconfigurational perturbation theory level. *Proc Natl Acad Sci USA* 101:17908–17913.
21. Lumento F, *et al.* (2007) Synthesis and characterization of a conformationally locked biomimetic photochemical switch. *Angew Chem Int Ed* 47:414–420.
22. Zanirato V, *et al.* (2007) Synthesis of biomimetic light-driven molecular switches via a cyclopropyl ring-opening/nitrilium ion ring-closing tandem reaction. *Tetrahedron* 63:4975–4982.
23. Fdez. Galván I, Sánchez ML, Martín ME, Olivares del Valle FJ, Aguilar MA (2003) Geometry optimization of molecules in solution: Joint use of the mean field approximation and the free-energy gradient method. *J Chem Phys* 118:255–263.
24. Frutos L-M, Andruniów T, Santoro F, Ferré N, Olivucci M (2007) Tracking the excited-state time evolution of the visual pigment with multiconfigurational quantum chemistry. *Proc Natl Acad Sci USA* 104:7764–7769.
25. Helbing J, *et al.*(2004) A fast photoswitch for minimally perturbed peptides: Investigation of the *trans* → *cis* photoisomerization of *N*-methylthioacetamide. *J Am Chem Soc* 126:8823–8834.
26. Klok M, *et al.* (2008) MHz unidirectional rotation of molecular rotary motors. *J Am Chem Soc* 130:10484–10485.
27. Roos BO (1987) in *Adv Chem Phys (Ab Initio Methods in Quantum Chemistry-II)*, ed Lawley KP (Wiley, New York), pp 399–446.
28. Andersson K, Malmqvist P-Å, Roos BO (1992) Second-order perturbation theory with a complete active space self-consistent field reference function. *J Chem Phys* 96:1218–1226.
29. Ferré N, Olivucci M (2003) Probing the rhodopsin cavity with reduced retinal models at the CASPT2//CASSCF/AMBER level of theory. *J Am Chem Soc* 125:6868–6869.
30. Zgrablić G, Voïtchovsky K, Kindermann M, Haacke S, Chergui M (2005) Ultrafast excited state dynamics of the protonated Schiff base of *all-trans* retinal in solvents. *Biophys J* 88:2779–2788.